ACS APPLIED NANO MATERIALS

www.acsanm.org

Article

Cation-Exchange Method Enables Uniform Iridium Oxide Nanospheres for Oxygen Evolution Reaction

Seongeun Park, Meital Shviro,* Heinrich Hartmann, Joachim Mayer, Marcelo Carmo, and Detlef Stolten

Cite This: *ACS Appl. Nano Mater.* 2022, 5, 4062−4071

Read Online

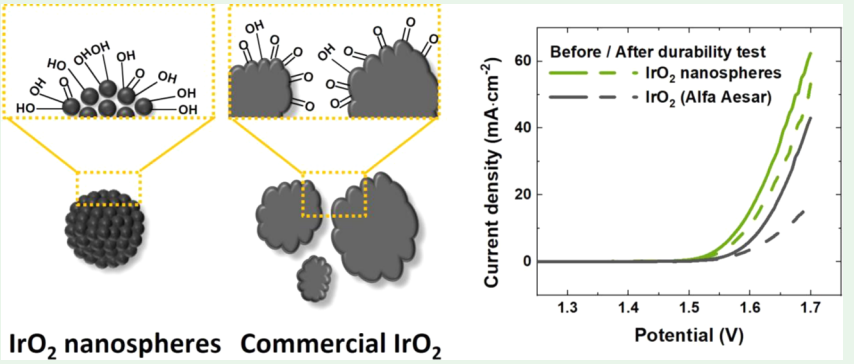

ABSTRACT: Polymer electrolyte membrane (PEM) water electrolyzers are a key technology for driving the energy system toward a renewable resource-based model. Numerous past and ongoing R&D activities have sought to reduce their dependence on precious metal catalysts, but unfortunately, there has still been no breakthrough in electrocatalyst design for PEM water electrolyzers. Scarce iridium remains the best choice as an electrocatalyst, thanks to its efficiency and durability for hosting the oxygen evolution reaction (OER). In this study, we present a synthesis method for preparing an iridium nanostructure that utilizes it more efficiently. A highly uniform morphology of IrO_2 nanospheres was achieved based on a cation-exchange reaction and using a sacrificial template. This highly simple synthesis enabled a high concentration of hydroxide groups on the surface without additional treatment to be achieved, which plays a significant role in enhancing OER, as electrocatalysts present a 3-fold increase in mass activity compared to commercial IrO_2. This study provides insights into the synthesis of nanostructures, with much potential to apply these to different applications. Moreover, we draw attention to the fundamental importance of structural properties with this simple but uniform structure and its performance as an electrocatalyst.

KEYWORDS: *iridium oxide, nanospheres, oxygen evolution reaction, electrolysis, cation exchange*

INTRODUCTION

Water electrolysis is an environmentally friendly technology for the production of hydrogen, which is considered a promising energy carrier for the near future. An electrolyzer splits water into oxygen and hydrogen using electricity, allowing the energy to be stored and the hydrogen to be used as a fuel or industrial feedstock. Polymer electrolyte membrane (PEM) water electrolysis has attracted particular attention as a means of producing green hydrogen due to its advantages compared to classic, alkaline-based systems, such as high current density, wider windows for a power input operation, and compact system design.[1] However, PEM water electrolyzers use a strong, solid acidic membrane as an electrolyte, and, together with high anodic over voltages, the materials used to split water must be highly resistant to the corrosive operating environment. Iridium oxide nanoparticles are recognized as the best and only practicable electrocatalysts for enabling the oxygen evolution reaction (OER), due to their superior electrocatalytic activity and durability under both acidic and oxidative conditions.[2−4] In recent decades, many researchers have searched for alternative catalyst materials to iridium,[5−7] but none of these have altered the state-of-the-art in the domain of commercial electrolyzer devices. As iridium is one of the rarest elements and therefore presents economic challenges, research into much higher utilization of iridium inside electrolysis cells is needed. In other words, iridium-based catalyst structures must be designed that allow the use of all iridium atoms during the OER, with iridium-based electrodes having 100% utilization.

Received: January 4, 2022
Accepted: February 18, 2022
Published: March 14, 2022

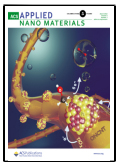

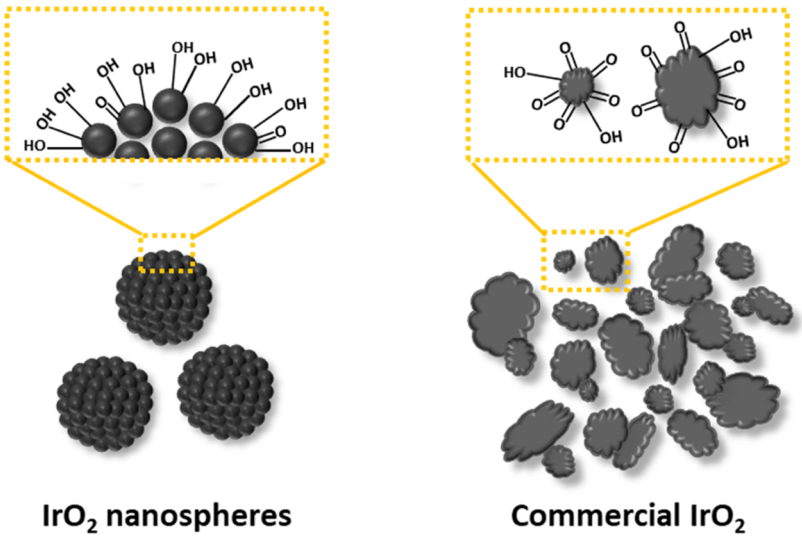

Figure 1. Schematic illustration of the synthesized IrO_2 nanospheres and commercial IrO_2.

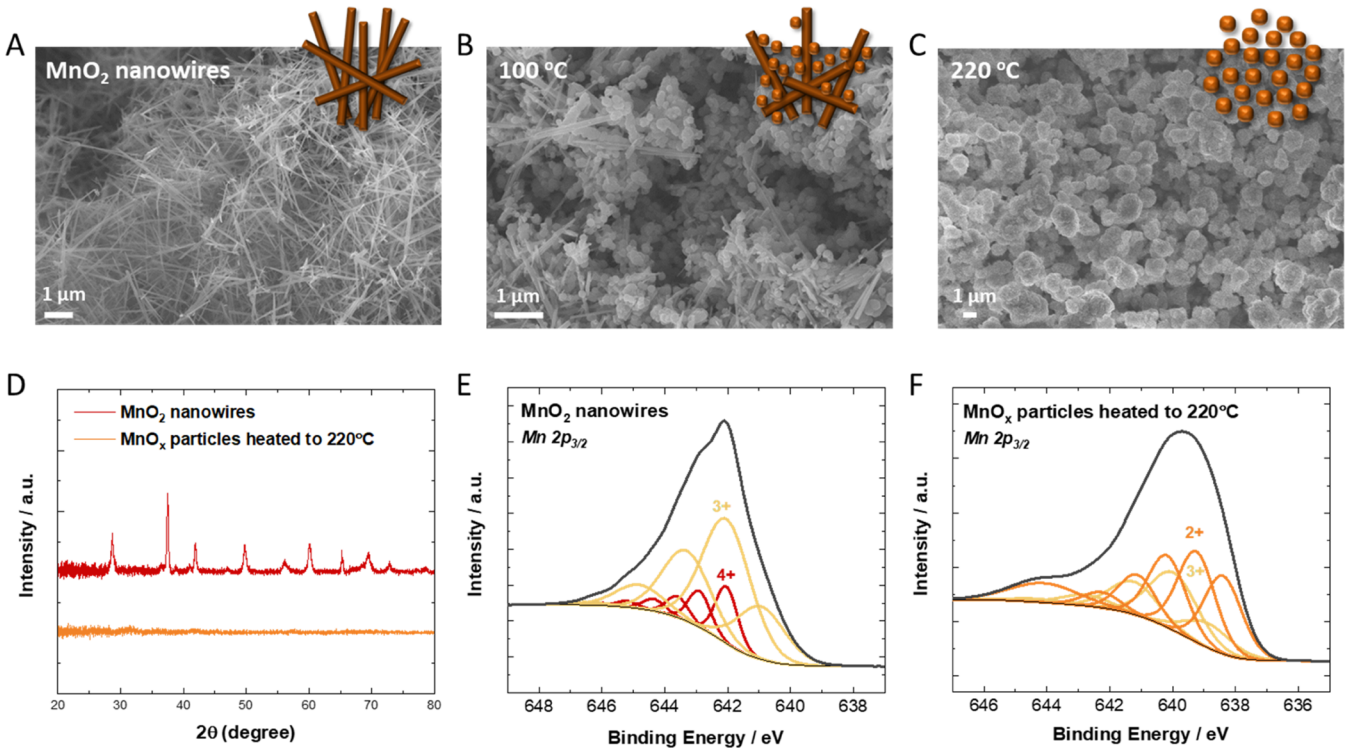

Figure 2. SEM images with corresponding illustrations of (A) MnO_2 nanowires and when it was heated to: (B) 100 °C, (C) 220 °C, (D) the XRD pattern, and (E, F) XPS spectra of MnO_2 nanowires and MnO_x particles after heating to 220 °C.

The fabrication of nanostructures is one of the most well-known strategies for improving electrocatalytic performance and utilization. Electrocatalytic performance can be improved in two ways: by increasing intrinsic catalytic activity or active surface area. Using nanosized materials is an easy way to increase the active surface area by exposing more surface area with a defined amount than microsized materials. The properties of nanostructures also depend on the size, shape, composition, arrangement of atoms, and more. In other words, controlling the shape of nanostructures can change the physical, chemical, and surface properties, which can improve intrinsic catalytic activity. Many types of nanostructures have been reported by various synthetic approaches, such as homogeneous nucleation,[8−10] seed-mediated growth,[11−13] galvanic replacement,[14−16] and others.[17−19] Using already prepared templates,[20−22] the design of nanostructures can be made more accurate. Moreover, the fabrication process can be better controlled by the separate synthesis procedure. Fan et al. presented various noble metal core−shell nanostructures by means of seed-mediated growth using different metal precursors with Au cores as the templates.[12] In turn, Han et al. demonstrated bimetallic hollow nanostructures by the galvanic replacement reaction using Cu seeds and investigated their structural diversity depending on the reaction conditions and different noble metal precursors.[14]

https://doi.org/10.1021/acsanm.2c00031
ACS Appl. Nano Mater. 2022, 5, 4062−4071

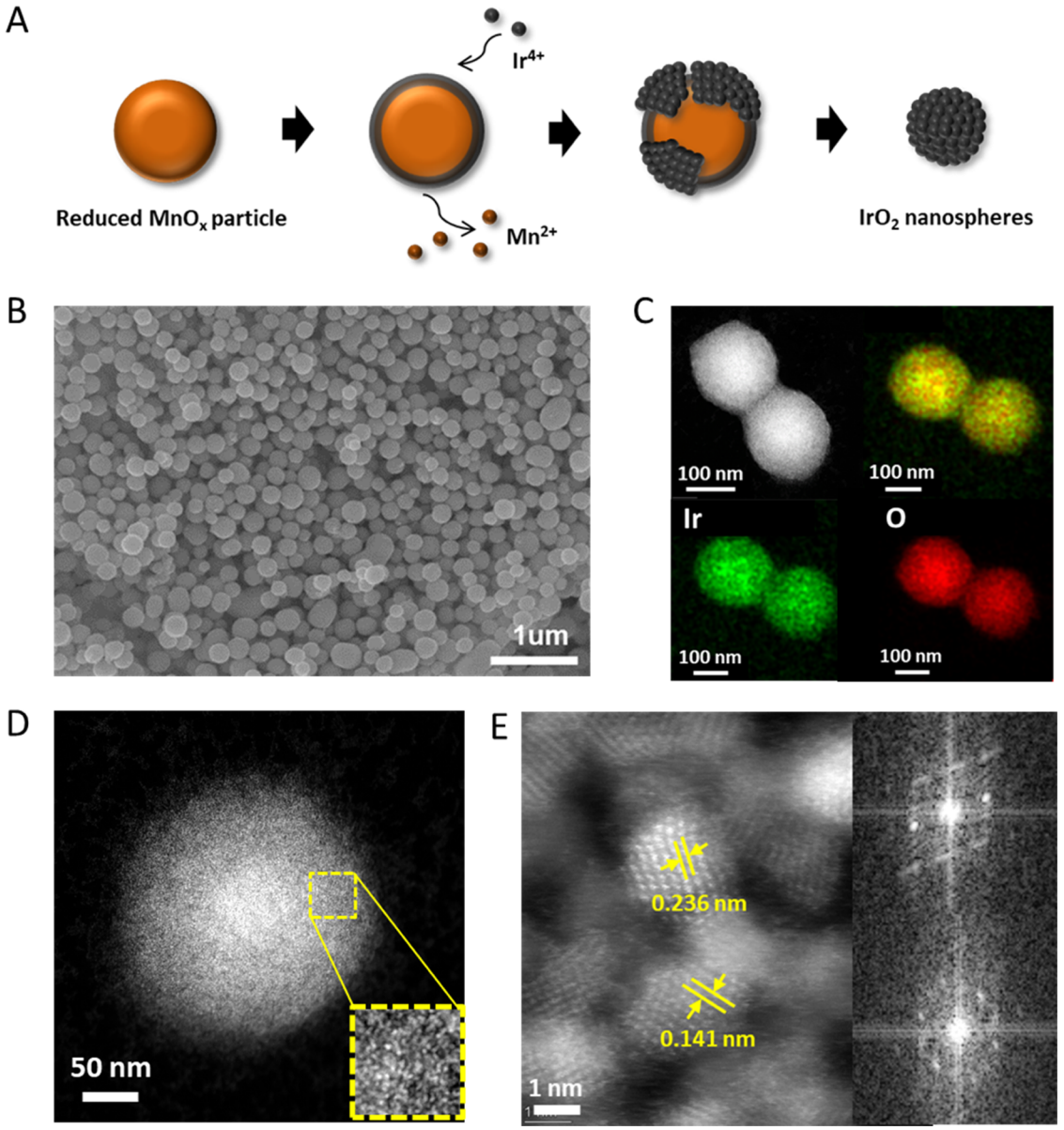

Figure 3. (A) Schematic illustration of the fabrication of IrO_2 nanospheres; (B) SEM characterization of IrO_2 nanospheres; (C) high-resolution HAADF-STEM image of IrO_2 nanospheres and corresponding elemental mapping with (D) enlarged image; and (E) high-resolution HAADF-STEM image and FFT patterns of IrO_2 nanoparticles.

Iridium has not been studied as extensively as the other metals mentioned above, as it is difficult to control its shape. For this reason, most iridium nanostructures reported in the literature were supported by additional elements to form an alloy or decoration of their surfaces.[23−25] Some studies have described the synthesis of iridium nanoparticles, but it is difficult to consider these as specific structures with a regularity,[26−28] or if they were only evaluated in basic conditions.[29] Therefore, to the best of our knowledge, hardly any studies have been published that also show structural effects with iridium structures for OER in acidic conditions.

In this study, we present a simple synthesis for the preparation of highly uniform IrO_2 nanospheres. These were synthesized via a cation-exchange reaction using MnO_2 as a based material. Here, the MnO_2 nanoparticle was used as an exchanged template with iridium. The successfully designed IrO_2 nanospheres were formed by assembling numerous small iridium oxide nanoparticles with spherical shapes with a 78.0% hydroxide content on the surface. In contrast, commercial IrO_2 usually agglomerates in irregular shapes and sizes and has a naturally oxidized surface covered by only 34.6% hydroxide. Figure 1 highlights the structural advantages and differences between commercial IrO_2 and the fabricated IrO_2 nanospheres. The evaluation of OER activity demonstrated a 3-fold improvement in the catalytic activity and stability of our IrO_2 nanospheres compared to commercial IrO_2. The improvement in electrochemical performance can be attributed to the structural uniformity and the generated hydroxide group on the surface of the IrO_2 nanospheres. Moreover, we present for the first time in detail the procedure for the preparation of IrO_2 nanospheres and explain the structural merits of the spheres obtained in this synthesis, which contributed to the improvement of the electrocatalytic performance. This study specifies the feasibility that can be applied to the syntheses of

https://doi.org/10.1021/acsanm.2c00031
ACS Appl. Nano Mater. 2022, 5, 4062−4071

other nanostructures by simply applying favorable materials for the cation-exchange reaction. It is intended to inspire the development of other noble metal-based nanomaterials that require sensitive conditions to be controlled for various applications, such as fuel cells, photovoltaics, sensors, and nanoparticles developed within agriculture and pharmaceutical applications.

RESULTS AND DISCUSSION

Structural Characterization. To design a well-controlled iridium oxide structure, MnO_2 was used as a template because it is easily achievable on large scale; moreover, it has been frequently reported for cation exchange.[30−32] The presence of the manganese template in this synthesis played an important role in the final morphology of iridium nanoparticles, as iridium nanoparticles barely showed a specific structure in the absence of MnO_2 (Figure S1). Initially, MnO_2 nanowires were formed by the hydrothermal method, which is described in detail in the Experimental Section. The MnO_2 nanowires transformed into spherical particles, while the reaction was heated to 220 °C (Figure 2). The thermodynamic properties of manganese oxide have been previously investigated.[33−35] Depending on the heat treatment and oxygen partial pressure, manganese oxide changes in terms of structure and morphology. In general, as the temperature increases, MnO_2 is reduced to Mn_2O_3, and Mn_2O_3 is reduced to MnO with structural transformation, and this reaction is accompanied by oxygen evolution. In our synthesis, the transformation could be facilitated because the heat treatment was carried out under Ar flow to obtain an inert atmosphere. The morphological change of our MnO_2 nanowires was observed by means of scanning electron microscopy (SEM), with a schematic illustration in the inset (Figure 2A−C). Initially, clear MnO_2 nanowires were apparent (Figure 2A), but during heating to 100 °C, some of these turned into roundish particles (Figure 2B). At the reaction temperature of 220 °C, the MnO_2 nanowires were fully transformed into aggregated round-shaped particles (Figure 2C). Additional analyses were performed to investigate the changes in the properties of the pristine MnO_2 nanowires and MnO_x particles heated at 220 °C (Figure 2D−F). Figure 2D compares the crystallinities measured by means of X-ray diffraction (XRD) for both materials. It indicates that the pristine MnO_2 nanowires have peaks matching the α-phase MnO_2 (JCPDS No.44−0141). In contrast, these became amorphous after being heated to 220 °C.

X-ray photoelectron spectroscopy (XPS) was used to determine the oxidation and chemical states (see Figure 2E,F). The pristine MnO_2 nanowires indicated that the majority of Mn^{4+} with 69.1 atom % and Mn^{3+} with 30.9 atom % were in the Mn $2p_{3/2}$ spectral region (Figure 2E). However, the MnO_x particles heated at 220 °C showed Mn^{3+} peaks that were weakened to 33.3 atom % and Mn^{2+} peaks intensified with 66.7 atom % of the higher ratio. This shows not only the formation of MnO but also the overall reduction of manganese from Mn^{4+} to Mn^{2+} induced by increasing the temperature. This reduction in the MnO_2 nanowires worked in favor of the cation-exchange reaction while considering the Pourbaix diagram for manganese (Figure S2). Below pH = 7, manganese prefers to exist as Mn^{2+} ions under zero potential. Given that the reaction solution was in the pH range of 3−5, due to the ascorbic acid used as a reducing agent and iridium precursor solution that will be subsequently added being a strongly acidic solution, it is apparent that manganese dissolves as Mn^{2+} ions. Accordingly, the change in the oxidation state to 2+ will accelerate the dissolution of manganese, which will, in turn, lead to the favorable cation exchange when iridium precursors are injected.

When the temperature reached 220 °C, the iridium precursor was injected into the solution and the cation-exchange reaction was initiated, as shown in Figure 3A. The MnO_x particles dissolved as Mn^{2+} ions, and the injected iridium ions were exchanged with Mn^{2+} ions via their kinetics at the reaction temperature, e.g., the energy allowed for the dissolution of manganese and precipitation of iridium.[36] In this reaction, poly(vinylpyrrolidone) (PVP) was used as a capping agent, which serves to restore the particles to a smaller, uniform shape by limiting their aggregation. As the reaction was proceeded in a closed system by wet chemistry, the intermediates could not be observed; however, inductively coupled plasma mass spectrometry (ICP-MS) was used to detect the dissolved manganese and provide evidence for the cation-exchange reaction. At the end of the synthesis, the first supernatant in the washing procedure was analyzed. As a result, 75% of the manganese participated in the reaction was detected in the first supernatant, proving that the manganese was successfully sacrificed and dissolved during the reaction. The remaining 25% of the manganese was detected in the subsequent washing steps.

The SEM image shown in Figure 3B presents the morphology of the synthesized IrO_2 nanospheres. It indicates that the IrO_2 nanospheres feature a size distribution of 201 ± 32 nm (Figure S3). High-angle annular dark-field scanning transmission electron microscopy (HAADF-STEM) confirmed the spherical shape, with an energy-dispersive X-ray (EDX) analysis revealing the evenly mixed iridium and oxygen within the structure (Figure 3C,D). No manganese was detected in the core, as the EDX value for manganese was less than 0.3 atom %. From the high-resolution HAADF-STEM images, it could be observed that the IrO_2 nanospheres are composed of 2 nm nanoparticles with a gap between them, suggesting that they are assembled utilizing a certain surface interaction, such as ligands that form on the surface during synthesis (Figure 3D). Fast Fourier transform (FFT) was applied to the high-resolution HAADF-STEM image, which observed (200) planes with the d-spacing 0.236 nm and (310), (112), and (301) planes with 0.141 nm value for iridium oxide (Figure 3E). XRD was used to verify the crystallinity of the IrO_2 nanospheres (Figure S4), and no diffraction peaks were detected. We note that this discrepancy between the XRD and TEM results regarding crystallinity could occur for nanoscale materials.[37,38] For nanomaterials below 50 nm, it is difficult to obtain a significant signal from the XRD measurement.[37] As the particle size decreases, the peaks become broader and the intensity can be attenuated. In particular, in the case of nanoparticles below 5 nm, it is highly challenging to distinguish crystallinity using only XRD. Furthermore, one should be careful when evaluating the results if the orientations of the particles are not in the same direction, as the mixed orientations can reduce the intensity of the resulting peaks due to misalignment.[37] Given that the IrO_2 nanospheres are composed of 2 nm iridium oxide nanoparticles in a random order, it is reasonable that they exhibit the amorphous pattern in the bulk XRD measurement.

XPS measurement was performed to determine the surface properties of the IrO_2 nanospheres and commercial IrO_2 (Figure 4). Figure 4A presents the XPS spectra in the Ir 4f

https://doi.org/10.1021/acsanm.2c00031
ACS Appl. Nano Mater. 2022, 5, 4062−4071

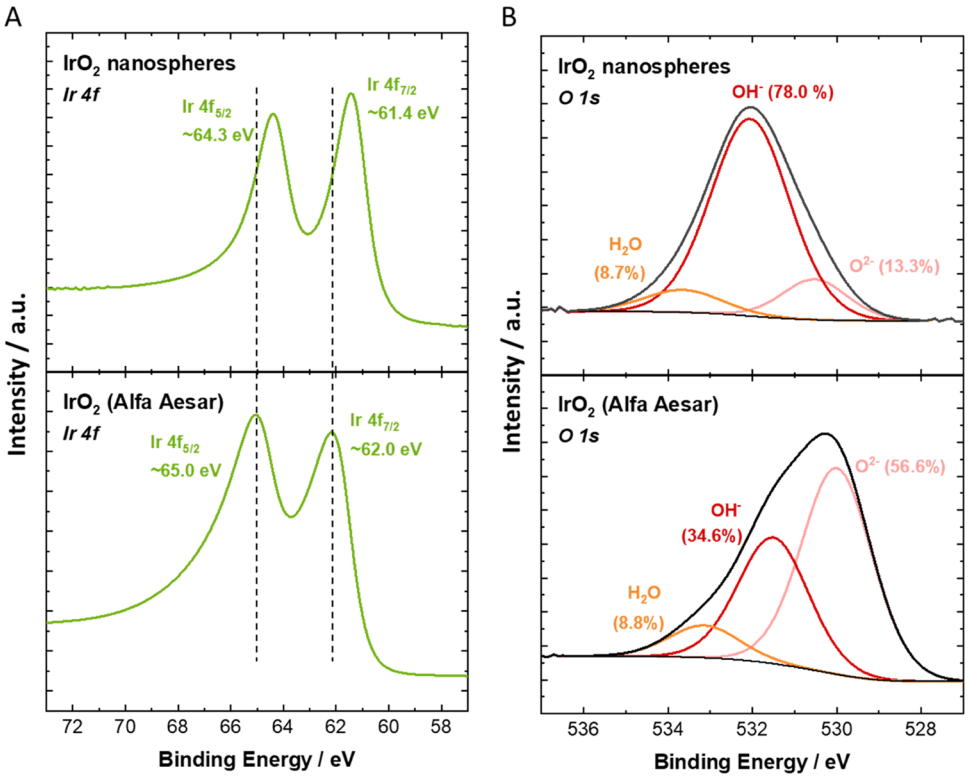

Figure 4. XPS spectra of the synthesized IrO_2 nanospheres and commercial IrO_2 (Alfa Aesar): (A) Ir 4f and (B) O 1s.

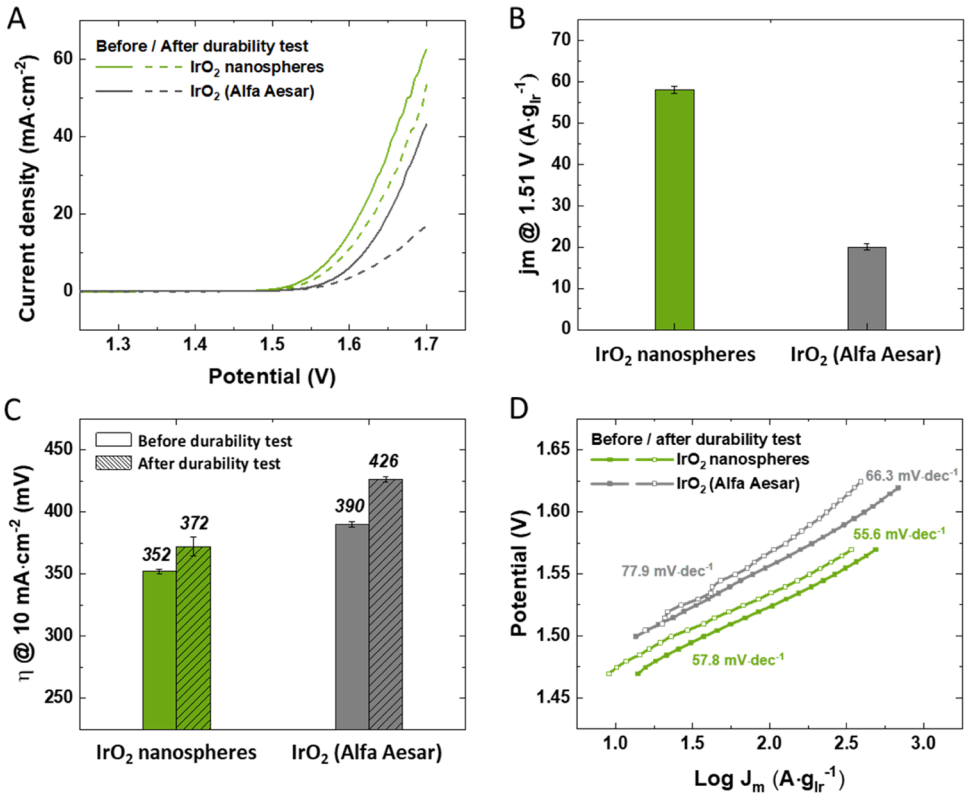

Figure 5. Electrochemical measurements of IrO_2 nanospheres by comparison with commercial IrO_2 (Alfa Aesar). (A) OER polarization curves measured in 0.5 mol·L^{-1} H_2SO_4 before and after chronoamperometry (CA) test for 5 h (till 1.6 V vs RHE); (B) Ir mass activities at 1.51 V (vs RHE); (C) bar graph displaying the overpotentials to drive 10 mA·cm^{-2}; and (D) Tafel plots before and after the CA test.

region, showing two main components of Ir $4f_{7/2}$ and Ir $4f_{5/2}$, which indicates that both materials have oxidized iridium peaks in the reported range for IrO_2, except that the doublets for IrO_2 nanospheres located in the slightly lower binding

https://doi.org/10.1021/acsanm.2c00031
ACS Appl. Nano Mater. 2022, 5, 4062−4071

energy.[39−42] The negatively shifted positions around 0.6 eV of IrO_2 nanospheres imply that the electronic structure of iridium was affected. On the contrary, the oxygen spectra exhibited considerably interesting results (Figure 4B). In the O 1s region, oxygen spectra can be deconvoluted into three peaks: (1) lattice oxygen (O^{2-}), (2) oxygen from hydroxide group (OH^-), and (3) adventitious oxygen usually related to adsorbed water. The IrO_2 nanospheres displayed a stronger hydroxide peak and lower oxide peak, with 78.0 and 13.3%, respectively, compared to commercial IrO_2 possessing 56.6% of oxide peak and 34.6% of hydroxide peak. The adventitious oxygen spectra were almost the same as 8.8 and 8.7%, which implies that the increased hydroxide portion of IrO_2 nanospheres is directly related to the decreased oxide. The increased hydroxide group could also explain the shift to the lower binding energy of Ir 4f doublets for IrO_2 nanospheres since the weaker bonding of the hydroxide group would substitute the stable divalent oxygen connected with iridium.[43]

Electrochemical Measurements. The IrO_2 nanospheres were evaluated as electrocatalysts for OER in a 0.5 $mol \cdot L^{-1}$ H_2SO_4 electrolyte. The electrochemically active surface area (ECSA) was measured and compared with commercial IrO_2. Since both materials have an oxidized surface, it was acquired by adopting the total anodic charges from the cyclic voltammetry (CV) profiles after the double layer corrected in the potential range of 0.4−1.25 V (vs RHE), and 440 $\mu C \cdot cm^{-2}$ was used as the electrical charge constant for the anodic processes.[44] To avoid the distortion of the result, the electrodes were swept from 0.05 to 1.53 V vs reversible hydrogen electrode (RHE) until the cyclic voltammogram was stable (Figure S5). The ECSA for IrO_2 nanospheres and the commercial IrO_2 were calculated as 16.45 and 20.43 $m^2 \cdot g_{Ir}^{-1}$, respectively. Despite the final particle size of around 200 nm, the reason that IrO_2 nanospheres could achieve the comparable ECSA value might be attributed to the more active surface property and morphological uniformity, as well as the reachable surface of iridium oxide nanoparticles inside of IrO_2 nanospheres. Brunauer−Emmett−Teller (BET) was also measured to compare with the calculated ECSA. It indicated 10.5 $m^2 \cdot g^{-1}$ for the synthesized IrO_2 nanospheres and 25.0 $m^2 \cdot g^{-1}$ for the commercial IrO_2, which showed a larger gap between the two materials than the values from ECSA measurement. Jung et al. studied 16 types of metal oxide nanoparticles and demonstrated that BET was not directly related to ECSA or electrocatalytic activity.[45] Ren et al. reported that the geometric area or BET surface area may not properly reflect the intrinsic electrocatalytic activity and ECSA can be the best way to compare the results by surface normalization techniques.[46] It is insisted that the discrepancy in the ECSA and BET results can originate from the difference between physical surface area and electrochemically active surface area of materials. Moreover, Stevens et al. reported that a more uniform surface area is a competent property for electrocatalysts as it increases the frequency of adsorption as electrocatalysts.[47] From this perspective, IrO_2 nanospheres actively use their surface area more efficiently than commercial IrO_2 as electrocatalysts.

Figure 5 shows the electrochemical performance of the IrO_2 nanospheres compared to commercial IrO_2. Prior to measuring OER performance, electrocatalyst coated on glassy carbon electrode was activated by potential sweeping between 0.4 and 1.4 V (vs RHE) at a scan rate of 500 $mV \cdot s^{-1}$ for 45 cycles. Activation was followed by CV for the same load range at a scan rate of 50 $mV \cdot s^{-1}$ to observe redox peaks. The commercial IrO_2 showed two oxidation peaks indicating oxidations of Ir(III) to Ir(IV) (∼0.8 V) and Ir(IV) to Ir(V) (∼1.2 V).[40,48,49] For the IrO_2 nanospheres, an exceptional oxidation peak was observed at ∼1.0 V (Figure S6), indicating not only the continuous oxidation of Ir(III) to Ir(V) but also the existence of hydrous oxide on the surface.[40] The OER activity was evaluated by linear sweep voltammetry (LSV) from 0.4 to 1.7 V (vs RHE) at a scan rate of 5 $mV \cdot s^{-1}$ in oxygen saturated electrolyte (Figure 5A). The IrO_2 nanospheres exhibited higher activity of 58 $A \cdot g_{Ir}^{-1}$ than commercial IrO_2 of 20 $A \cdot g_{Ir}^{-1}$ at 1.51 V, which corresponds to an ∼3-fold improvement in activity (Figure 5B). This is a significant increase as an electrocatalyst composed of iridium only, considering the reported iridium oxide materials (Table S1). When the activities were normalized with the achieved ECSA, the IrO_2 nanospheres and commercial IrO_2 showed 0.353 and 0.098 $mA \cdot cm_{ECSA}^{-2}$, respectively, indicating a 3.6-fold improvement in activity for the IrO_2 nanospheres. We attribute this improvement to the structural advantages of the IrO_2 nanospheres, such as the morphological uniformity in shape and size, as well as the generated hydroxide group on their surface during synthesis. Considering the irregular shapes of commercial iridium nanoparticles,[3] they are known to agglomerate and cause low efficient porosity and surface utilization due to the uneven shape and size distribution, whereas the uniform morphology of IrO_2 nanospheres can expose the surface more efficiently, which promotes the catalytic reaction.[50−54] As previously shown, particle size distribution is closely related to catalytic activity and stability and has been demonstrated on Pt/C nanoparticles.[50] Moreover, a wide size distribution of particles causes electrode polarization, which is associated with degradation and poor electrochemical performance.[51]

As presented in the XPS results, the hydroxide group was generated during the synthesis of IrO_2 nanospheres. The hydroxide group is well known as playing an influential role in enhancing electrocatalytic activity.[2,39,43,55−57] Abbott et al. demonstrated that the enhancement of OER activity was related to the initial hydroxide layer.[39] The effects of particle size, morphology, and surface area were investigated using four types of synthesized IrO_2, and it was found that the intrinsic catalytic activity correlated most strongly with the hydroxide group on the surface. Alia et al. reported that the hydroxide group, which is released when the alloyed transition metal is leached, can enhance the catalytic activity.[2] The synthesized Ir−Ni and Ir−Co nanowires were leached via ex situ acid treatment and resulted in 11- and 8-fold enhanced activity, respectively. Here, we point out that the hydroxide group on the surface can be achieved without additional leaching treatment. It implies that a well-designed synthesis can avoid further experimental steps and prevent degradation due to the dissolution of transition metals that are not perfectly leached. Moreover, Casalongue et al. observed the surface of iridium oxide nanoparticles during OER by in situ ambient pressure XPS and proved that the OER takes place when the hydroxide on the catalyst surface converts to oxide.[58] Based on these previous studies, the enhanced electrocatalytic activity of IrO_2 nanospheres is here strongly correlated with the increased hydroxide group on the surface.

We evaluated the initial stability of both catalysts by applying a constant potential of 1.6 V (vs RHE) for 5 h, following the protocols established by different research

https://doi.org/10.1021/acsanm.2c00031
ACS Appl. Nano Mater. 2022, 5, 4062−4071

groups.[44,59,60] The OER polarization curves after the 5 h test are shown as dashed lines in Figure 5A, and the overpotentials to obtain 10 mA·cm^{-2} before and after the durability test are compared in Figure 5C. The overpotential of the IrO_2 nanospheres was 352 mV and increased by 5.7% after the durability test. In contrast, the overpotential of the commercial IrO_2 was increased by 9.2% from 390 to 426 mV. To understand the kinetic behavior of the electrocatalysts, the Tafel plots from the OER activities before and after the durability test were analyzed (Figure 5D). The IrO_2 nanospheres showed 57.8 mV·dec^{-1} of the initial Tafel slope that is the generally reported value for iridium materials (~60 mV·dec^{-1}), implying that the OER is mainly determined by the step to convert to the "activated hydroxide group (−OH)."[61−63] The Tafel slope hardly changed after the durability test (55.6 mV·dec^{-1}). In contrast, the commercial IrO_2 indicated a higher Tafel slope of 66.3 mV·dec^{-1} than IrO_2 nanospheres, which degraded to 77.9 mV·dec^{-1} after 5 h. In particular, it showed highly unstable plots before it started to be kinetically controlled (<1.55 V). These results suggest that the electrochemical conditions for the durability test affected the stability of the commercial IrO_2. We speculate that it is related to the morphological vulnerability of commercial IrO_2 since it is favorable to particle aggregation and ripening.[64,65] Moreover, the morphology of IrO_2 nanospheres after the durability test by HAADF-STEM (Figure S7) was analyzed, and it showed that the IrO_2 nanospheres were disassembled into small nanoparticles, rather than agglomeration. The reason can be attributed to that the ligand or covalent bonds connecting between the small particles were decomposed electrochemically during the measurement and it could be correlated to the dismantling of IrO_2 nanospheres. The electrochemical potential causes various structural changes and destruction,[66−68] as shown by Huang et al. small Cu nanoparticles (~3 nm) were detached from Cu nanocubes during CO_2 reduction.[66] Beermann et al. observed the structural degradation of Pt−Ni octahedral from selective dissolution to recoarsening using an in situ electrochemical cell.[67] Such degradation mechanisms in catalyst structures can be continued to the loss of ECSA.[44,69] Contrary to the small nanoparticles that easily agglomerate and lose their surface area during electrochemical measurements, a superstructure of IrO_2 nanospheres can be rather beneficial to maintain the electrochemical stability by suppressing the agglomeration of electrocatalysts. Accordingly, when considering the Tafel slopes and morphological change, it is interpreted that the degradation observed in OER activity for IrO_2 nanospheres is the loss of catalysts amount on the electrode during measurements, rather than the weakened catalytic activity of electrocatalyst itself, which can be resolved by modifying the bonding between nanoparticles or applying it onto the electrode.

CONCLUSIONS

In this study, uniform IrO_2 nanospheres were synthesized through a cation-exchange reaction based on an indispensable sacrificial template. MnO_2 was used as a template and fully exchanged with iridium and dissolved as ions during the synthesis. Uniform IrO_2 nanospheres were achieved, and these were confirmed as well-organized assembled nanostructures by the presence of countless small iridium oxide nanoparticles with high crystallinity. In the surface characterization analysis, it was found that the hydroxide group on the surface of the IrO_2 nanospheres was generated during synthesis. The IrO_2 nanospheres were evaluated as electrocatalysts for OER under acidic conditions and exhibited 3-fold enhanced mass activity at 1.51 V (58 A·g_{Ir}^{-1}) compared to that of commercial IrO_2 (20 A·g_{Ir}^{-1}). Moreover, 3.5% featured improved stability at 1.6 V for 5 h, which can be improved upon when tested under similar conditions in a real cell by limiting the physical loss of IrO_2 nanospheres during measurements. Based on the comparison study between synthesized IrO_2 nanospheres and commercial IrO_2, the improved performance of IrO_2 nanospheres could be attributed to structural advantages such as morphological uniformity and increased hydroxide content on the surface. In particular, considering the changed aspects of both catalysts following the electrochemical measurements, IrO_2 nanospheres did not electrochemically deteriorate, unlike the commercial IrO_2. Therefore, we consider the IrO_2 nanospheres to be of high R&D potential. As research on the iridium structure itself is scarce, these results support the importance of addressing structural uniformity for materials as electrocatalysts. Furthermore, this study demonstrated that it is possible to achieve the hydroxide group on the catalyst surface during synthesis without post-treatment. We believe that this synthesis can provide a guide and strategy for the more efficient fabrication of nanostructures based on the cation exchange by adjusting the kinetics of the materials, as it offers wide-ranging opportunities for further investigation and development of improved nanostructures by controlling the experimental conditions. It also highlights the fundamental importance of the structural properties of the materials used in many applications.

EXPERIMENTAL SECTION

Materials. Potassium permanganate ($KMnO_4$, 99.0%, Sigma-Aldrich), hydrochloric acid (HCl, 37%, Alfa Aesar), ethanol (99.8%, MERCK), poly(vinylpyrrolidone) (PVP, M.W. 58k, Alfa Aesar), L-ascorbic acid (99.7%, Sigma-Aldrich), ethylene glycol (EG, Merck), dihydrogen hexachloroiridate(IV) hydrate (H_2IrCl_6, 99%, Alfa Aesar), and acetone (99%, MERCK) were used without additional purification.

Synthesis of α-MnO_2 Nanowires. Typically, 2.8 mmol of $KMnO_4$ was dissolved in DI water with the addition of 11.2 mmol of HCl. A total of 60 mL of solution was stirred for 20 min and transferred to a Teflon autoclave cell. The solution was heated to 240 °C and kept for 3 h. After 3 h, the solution was cooled down naturally to room temperature and washed with ethanol and DI water by vacuum filtration. The obtained dark brownish precipitates were dried overnight under vacuum conditions.

Synthesis of IrO_2 Nanospheres. The well-assembled IrO_2 nanospheres were fabricated by the polyol method. For the first step, 0.009 mmol of PVP and 1.7 mmol of L-ascorbic acid were mixed with 25 mL of EG in a Schlenk flask (volume: 250 mL). The materials were vigorously stirred in a preheated oil bath at 100 °C with Ar flowing. After 1 h, α-MnO_2 nanowires dispersed in 25 mL of EG added, followed by heating to 220 °C. At 220 °C, H_2IrCl_6 dissolved in 15 mL of EG and injected. The reaction was kept for 1 h and cooled down naturally. After the solution cooled down to room temperature, the content was washed with ethanol and acetone by centrifugation until the transparent supernatant was achieved. The dark precipitates were dried overnight under vacuum conditions.

Morphological, Structural, and Elemental Characterization. Scanning electron microscopy (SEM) was conducted on Hitachi SU8000 at an accelerating voltage of 15 kV. Scanning transmission electron microscopy (STEM) and energy-dispersive X-ray spectroscopy (EDX) investigations were conducted using an FEI (Thermo Fisher Scientific) Titan 80-200 electron microscope.[70] To achieve "Z-contrast" conditions, a probe semiangle of 26 mrad was used with the

https://doi.org/10.1021/acsanm.2c00031
ACS Appl. Nano Mater. 2022, 5, 4062−4071

detector having a 75 mrad inner collection angle. For the EDX elemental mapping, Ir L, O K, and Mn K peaks were utilized. X-ray diffractions (XRD) were measured in D8 DISCOVER (Bruker) using a Cu Ka source and LYNXEYE_XE_T as a detector. X-ray photoelectron spectroscopy was performed on a PHI 5000 Versaprobe II instrument with a monochromatic Al K α X-ray source. The powder samples were pressed onto indium foil, which was fixed with clamps on a stainless steel sample holder. The core-level spectra were recorded with a pass energy of 23.5 eV, 0.1 eV energy step, and a spot size of 200 μm. An electron flood gun and an Ar^+ ion gun were used for charge compensation. The spectra were charge corrected by setting the binding energy of the main C 1s component to 285 eV. Inductively coupled plasma mass spectrometry (ICP-MS) of the supernatant in the washing procedure after synthesis was measured in Agilent 7900.

Electrochemical Measurements. For the electrochemical measurements, a typical three-electrode setup was used with a reversible hydrogen electrode (RHE) as the reference electrode and a Pt mesh rod as the counter electrode. A glassy carbon (GC) electrode (diameter: 5 mm, area: 0.196 cm^2) served as the working electrode. For this working electrode, the ink was prepared by mixing the 3.5 mg of catalysts with 0.7 mg of Vulcan X-72 in DI water (7.6 mL), ethanol (2.4 mL), and 5% Nafion (40 μL). The mixture was sonicated for 30 min to form a homogeneous ink. In this case, 10 μL of the well-dispersed ink was dropped on the GC and dried naturally at room temperature. The loading amount of catalyst on the GC was calculated to be 17.8 $\mu g\ cm^{-2}$. The cell was purged with N_2 gas before starting the measurements. Cyclic voltammetry was performed between +0.4 and +1.4 V with a scan rate of 50 mV s^{-1}. Linear sweep voltammetry was recorded from +0.4 to +1.7 V with a scan rate of 5 mV s^{-1} at O_2 saturation.

■ ASSOCIATED CONTENT

Supporting Information

The Supporting Information is available free of charge at https://pubs.acs.org/doi/10.1021/acsanm.2c00031.

Additional HAADF-STEM image of iridium product when the reaction is proceeded without manganese material; Pourbaix diagram of manganese; additional SEM image and particle size distribution of IrO_2 nanospheres; XRD pattern of IrO_2 nanospheres; cyclic voltammograms for the ECSA measurement; cyclic voltammograms for the synthesized IrO_2 nanospheres and commercial IrO_2 nanoparticles; comparison of OER performance with other reported iridium oxide materials; and high-resolution HAADF-STEM images of IrO_2 nanospheres with elemental mapping for iridium (red) and oxygen (green) after the CA test for 5 h (PDF)

■ AUTHOR INFORMATION

Corresponding Author

Meital Shviro − *Institute of Energy and Climate Research, Electrochemical Process Engineering (IEK-14), Forschungszentrum Jülich GmbH, 52425 Jülich, Germany;* orcid.org/0000-0002-9494-0233; Email: m.shviro@fz-juelich.dem

Authors

Seongeun Park − *Institute of Energy and Climate Research, Electrochemical Process Engineering (IEK-14), Forschungszentrum Jülich GmbH, 52425 Jülich, Germany*

Heinrich Hartmann − *Central Institute for Engineering, Electronics and Analytics (ZEA-3), Forschungszentrum Jülich GmbH, 52425 Jülich, Germany*

Joachim Mayer − *ER-C 2, Forschungszentrum Jülich GmbH, 52425 Jülich, Germany; GFE, RWTH Aachen University, 52074 Aachen, Germany*

Marcelo Carmo − *Institute of Energy and Climate Research, Electrochemical Process Engineering (IEK-14), Forschungszentrum Jülich GmbH, 52425 Jülich, Germany; Mechanical and Materials Engineering, Queen's University, Kingston, Ontario K7L 3N6, Canada;* orcid.org/0000-0002-0186-317X

Detlef Stolten − *Institute of Energy and Climate Research, Techno-economic Systems Analysis (IEK-3), Forschungszentrum Jülich GmbH, 52425 Jülich, Germany; Chair for Fuel Cells, RWTH Aachen University, 52062 Aachen, Germany*

Complete contact information is available at: https://pubs.acs.org/10.1021/acsanm.2c00031

Notes

The authors declare no competing financial interest.

■ ACKNOWLEDGMENTS

M.S. thanks the Alexander von Humboldt Foundation for financial support.

■ REFERENCES

(1) Carmo, M.; Fritz, D. L.; Mergel, J.; Stolten, D. A Comprehensive Review on PEM Water Electrolysis. *Int. J. Hydrogen Energy* **2013**, *38*, 4901−4934.

(2) Alia, S. M.; Shulda, S.; Ngo, C.; Pylypenko, S.; Pivovar, B. S. Iridium-Based Nanowires as Highly Active, Oxygen Evolution Reaction Electrocatalysts. *ACS Catal.* **2018**, *8*, 2111−2120.

(3) Rakousky, C.; Shviro, M.; Carmo, M.; Stolten, D. Iridium Nanoparticles for the Oxygen Evolution Reaction: Correlation of Structure and Activity of Benchmark Catalyst Systems. *Electrochim. Acta* **2019**, *302*, 472−477.

(4) Liu, C.; Shviro, M.; Gago, A. S.; Zaccarine, S. F.; Bender, G.; Gazdzicki, P.; Morawietz, T.; Biswas, I.; Rasinski, M.; Everwand, A.; Schierholz, R.; Pfeilsticker, J.; Müller, M.; Lopes, P. P.; Eichel, R.; Pivovar, B.; Pylypenko, S.; Friedrich, K. A.; Lehnert, W.; Carmo, M. Exploring the Interface of Skin-Layered Titanium Fibers for Electrochemical Water Splitting. *Adv. Energy Mater.* **2021**, *11*, No. 2002926.

(5) Ledendecker, M.; Krickcalderõn, S.; Papp, C.; Steinrück, H. P.; Antonietti, M.; Shalom, M. The Synthesis of Nanostructured Ni5P4 Films and Their Use as a Non-Noble Bifunctional Electrocatalyst for Full Water Splitting. *Angew. Chem., Int. Ed.* **2015**, *54*, 12361−12365.

(6) Dou, Y.; Liao, T.; Ma, Z.; Tian, D.; Liu, Q.; Xiao, F.; Sun, Z.; Ho Kim, J.; Xue Dou, S. Graphene-like Holey Co3O4 Nanosheets as a Highly Efficient Catalyst for Oxygen Evolution Reaction. *Nano Energy* **2016**, *30*, 267−275.

(7) Mondschein, J. S.; Callejas, J. F.; Read, C. G.; Chen, J. Y. C.; Holder, C. F.; Badding, C. K.; Schaak, R. E. Crystalline Cobalt Oxide Films for Sustained Electrocatalytic Oxygen Evolution under Strongly Acidic Conditions. *Chem. Mater.* **2017**, *29*, 950−957.

(8) Wang, Y.; Peng, H. C.; Liu, J.; Huang, C. Z.; Xia, Y. Use of Reduction Rate as a Quantitative Knob for Controlling the Twin Structure and Shape of Palladium Nanocrystals. *Nano Lett.* **2015**, *15*, 1445−1450.

(9) Biacchi, A. J.; Schaak, R. E. The Solvent Matters: Kinetic versus Thermodynamic Shape Control in the Polyol Synthesis of Rhodium Nanoparticles. *ACS Nano* **2011**, *5*, 8089−8099.

(10) Zhou, M.; Wang, H.; Vara, M.; Hood, Z. D.; Luo, M.; Yang, T. H.; Bao, S.; Chi, M.; Xiao, P.; Zhang, Y.; Xia, Y. Quantitative Analysis of the Reduction Kinetics Responsible for the One-Pot Synthesis of Pd-Pt Bimetallic Nanocrystals with Different Structures. *J. Am. Chem. Soc.* **2016**, *138*, 12263−12270.

(11) Lim, B.; Wang, J.; Camargo, P. H. C.; Jiang, M.; Kim, M. J.; Xia, Y. Facile Synthesis of Bimetallic Nanoplates Consisting of Pd Cores and Pt Shells through Seeded Epitaxial Growth. *Nano Lett.* **2008**, *8*, 2535−2540.
(12) Fan, F. R.; Liu, D. Y.; Wu, Y. F.; Duan, S.; Xie, Z. X.; Jiang, Z. Y.; Tian, Z. Q. Epitaxial Growth of Heterogeneous Metal Nanocrystals: From Gold Nano-Octahedra to Palladium and Silver Nanocubes. *J. Am. Chem. Soc.* **2008**, *130*, 6949−6951.
(13) Habas, S. E.; Lee, H.; Radmilovic, V.; Somorjai, G. A.; Yang, P. Shaping Binary Metal Nanocrystals through Epitaxial Seeded Growth. *Nat. Mater.* **2007**, *6*, 692−697.
(14) Han, L.; Wang, P.; Liu, H.; Tan, Q.; Yang, J. Balancing the Galvanic Replacement and Reduction Kinetics for the General Formation of Bimetallic CuM (M = Ru, Rh, Pd, Os, Ir, and Pt) Hollow Nanostructures. *J. Mater. Chem. A* **2016**, *4*, 18354−18365.
(15) Sun, X.; Kim, J.; Gilroy, K. D.; Liu, J.; König, T. A. F.; Qin, D. Gold-Based Cubic Nanoboxes with Well-Defined Openings at the Corners and Ultrathin Walls Less Than Two Nanometers Thick. *ACS Nano* **2016**, *10*, 8019−8025.
(16) Slater, T. J. A.; Macedo, A.; Schroeder, S. L. M.; Burke, M. G.; O'Brien, P.; Camargo, P. H. C.; Haigh, S. J. Correlating Catalytic Activity of Ag-Au Nanoparticles with 3D Compositional Variations. *Nano Lett.* **2014**, *14*, 1921−1926.
(17) Luo, S.; Shen, P. K. Concave Platinum-Copper Octopod Nanoframes Bounded with Multiple High-Index Facets for Efficient Electrooxidation Catalysis. *ACS Nano* **2017**, *11*, 11946−11953.
(18) Okazaki, K.; Yasui, J.; Torimoto, T. Electrochemical Deposition of Gold Frame Structure on Silver Nanocubes. *Chem. Commun.* **2009**, *104*, 2917.
(19) Park, S.; Shviro, M.; Hartmann, H.; Besmehn, A.; Mayer, J.; Stolten, D.; Carmo, M. Nickel Structures as a Template Strategy to Create Shaped Iridium Electrocatalysts for Electrochemical Water Splitting. *ACS Appl. Mater. Interfaces* **2021**, *13*, 13576−13585.
(20) Jiang, B.; Kim, J.; Guo, Y.; Wu, K. C. W.; Alshehri, S. M.; Ahamad, T.; Alhokbany, N.; Henzie, J.; Yamachi, Y. Efficient Oxygen Evolution on Mesoporous IrOx Nanosheets. *Catal. Sci. Technol.* **2019**, *9*, 3697−3702.
(21) Leteba, G. M.; Mitchell, D. R. G.; Levecque, P. B. J.; Macheli, L.; Van Steen, E.; Lang, C. I. High-Index Core-Shell Ni-Pt Nanoparticles as Oxygen Reduction Electrocatalysts. *ACS Appl. Nano Mater.* **2020**, *3*, 5718−5731.
(22) Jiang, B.; Guo, Y.; Kim, J.; Whitten, A. E.; Wood, K.; Kani, K.; Rowan, A. E.; Henzie, J.; Yamauchi, Y. Mesoporous Metallic Iridium Nanosheets. *J. Am. Chem. Soc.* **2018**, *140*, 12434−12441.
(23) Xia, X.; Figueroa-Cosme, L.; Tao, J.; Peng, H.-C.; Niu, G.; Zhu, Y.; Xia, Y. Facile Synthesis of Iridium Nanocrystals with Well-Controlled Facets Using Seed-Mediated Growth. *J. Am. Chem. Soc.* **2014**, *136*, 10878−10881.
(24) Kwon, T.; Hwang, H.; Sa, Y. J.; Park, J.; Baik, H.; Joo, S. H.; Lee, K. Cobalt Assisted Synthesis of IrCu Hollow Octahedral Nanocages as Highly Active Electrocatalysts toward Oxygen Evolution Reaction. *Adv. Funct. Mater.* **2017**, *27*, No. 1604688.
(25) Wang, C.; Sui, Y.; Xiao, G.; Yang, X.; Wei, Y.; Zou, G.; Zou, B. Synthesis of Cu−Ir Nanocages with Enhanced Electrocatalytic Activity for the Oxygen Evolution Reaction. *J. Mater. Chem. A* **2015**, *3*, 19669−19673.
(26) Zhao, Y.; Hernandez-Pagan, E. A.; Vargas-Barbosa, N. M.; Dysart, J. L.; Mallouk, T. E. A High Yield Synthesis of Ligand-Free Iridium Oxide Nanoparticles with High Electrocatalytic Activity. *J. Phys. Chem. Lett.* **2011**, *2*, 402−406.
(27) Willinger, E.; Massué, C.; Schlögl, R.; Willinger, M. G. Identifying Key Structural Features of IrOx Water Splitting Catalysts. *J. Am. Chem. Soc.* **2017**, *139*, 12093−12101.
(28) Bizzotto, F.; Quinson, J.; Zana, A.; Kirkensgaard, J. J. K.; Dworzak, A.; Oezaslan, M.; Arenz, M. Ir Nanoparticles with Ultrahigh Dispersion as Oxygen Evolution Reaction (OER) Catalysts: Synthesis and Activity Benchmarking. *Catal. Sci. Technol.* **2019**, *9*, 6345−6356.
(29) Ahmed, J.; Mao, Y. Ultrafine Iridium Oxide Nanorods Synthesized by Molten Salt Method toward Electrocatalytic Oxygen and Hydrogen Evolution Reactions. *Electrochim. Acta* **2016**, *212*, 686−693.
(30) Hua, K.; Li, X.; Fu, Z.; Fang, D.; Bao, R.; Yi, J.; Luo, Z. Cation-Exchange Synthesis of Manganese Vanadate Nanosheets and Its Application in Lithium-Ion Battery. *J. Solid State Chem.* **2019**, *273*, 287−294.
(31) Luo, Z.; Irtem, E.; Ibánez, M.; Nafria, R.; Marti-Sánchez, S.; Genç, A.; De La Mata, M.; Liu, Y.; Cadavid, D.; Llorca, J.; Arbiol, J.; Andreu, T.; Morante, J. R.; Cabot, A. Mn3O4@CoMn2O4-CoxOy Nanoparticles: Partial Cation Exchange Synthesis and Electrocatalytic Properties toward the Oxygen Reduction and Evolution Reactions. *ACS Appl. Mater. Interfaces* **2016**, *8*, 17435−17444.
(32) Lentijo-Mozo, S.; Deiana, D.; Sogne, E.; Casu, A.; Falqui, A. Unexpected Insights about Cation-Exchange on Metal Oxide Nanoparticles and Its Effect on Their Magnetic Behavior. *Chem. Mater.* **2018**, *30*, 8099−8112.
(33) Fritsch, S.; Navrotsky, A. Thermodynamic Properties of Manganese Oxides. *J. Am. Ceram. Soc.* **1996**, *79*, 1761−1768.
(34) Jacob, K. T.; Kumar, A.; Rajitha, G.; Waseda, Y. Thermodynamic Data for Mn 3O 4, Mn 2O 3 and MnO 2. *High Temp. Mater. Processes* **2011**, *30*, 459−472.
(35) Deljoo, B.; Tan, H.; Suib, S. L.; Aindow, M. Thermally Activated Structural Transformations in Manganese Oxide Nanoparticles under Air and Argon Atmospheres. *J. Mater. Sci.* **2020**, *55*, 7247−7258.
(36) Rivest, J. B.; Jain, P. K. Cation Exchange on the Nanoscale: An Emerging Technique for New Material Synthesis, Device Fabrication, and Chemical Sensing. *Chem. Soc. Rev.* **2013**, *42*, 89−96.
(37) Holder, C. F.; Schaak, R. E. Tutorial on Powder X-Ray Diffraction for Characterizing Nanoscale Materials. *ACS Nano* **2019**, *13*, 7359−7365.
(38) Moreau, L. M.; Ha, D. H.; Zhang, H.; Hovden, R.; Muller, D. A.; Robinson, R. D. Defining Crystalline/Amorphous Phases of Nanoparticles through X-Ray Absorption Spectroscopy and X-Ray Diffraction: The Case of Nickel Phosphide. *Chem. Mater.* **2013**, *25*, 2394−2403.
(39) Abbott, D. F.; Lebedev, D.; Waltar, K.; Povia, M.; Nachtegaal, M.; Fabbri, E.; Copéret, C.; Schmidt, T. J. Iridium Oxide for the Oxygen Evolution Reaction: Correlation between Particle Size, Morphology, and the Surface Hydroxo Layer from Operando XAS. *Chem. Mater.* **2016**, *28*, 6591−6604.
(40) Chen, Y.; Li, H.; Wang, J.; Du, Y.; Xi, S.; Sun, Y.; Sherburne, M.; Ager, J. W.; Fisher, A. C.; Xu, Z. J. Exceptionally Active Iridium Evolved from a Pseudo-Cubic Perovskite for Oxygen Evolution in Acid. *Nat. Commun.* **2019**, *10*, No. 572.
(41) Date, N. S.; Hengne, A. M.; Huang, K. W.; Chikate, R. C.; Rode, C. V. Single Pot Selective Hydrogenation of Furfural to 2-Methylfuran over Carbon Supported Iridium Catalysts. *Green Chem.* **2018**, *20*, 2027−2037.
(42) Pfeifer, V.; Jones, T. E.; Velasco Vélez, J. J.; Massué, C.; Greiner, M. T.; Arrigo, R.; Teschner, D.; Girgsdies, F.; Scherzer, M.; Allan, J.; Hashagen, M.; Weinberg, G.; Piccinin, S.; Hävecker, M.; Knop-Gericke, A.; Schlögl, R. The Electronic Structure of Iridium Oxide Electrodes Active in Water Splitting. *Phys. Chem. Chem. Phys.* **2016**, *18*, 2292−2296.
(43) Reier, T.; Pawolek, Z.; Cherevko, S.; Bruns, M.; Jones, T.; Teschner, D.; Selve, S.; Bergmann, A.; Nong, H. N.; Schlögl, R.; Mayrhofer, K. J. J.; Strasser, P. Molecular Insight in Structure and Activity of Highly Efficient, Low-Ir Ir−Ni Oxide Catalysts for Electrochemical Water Splitting (OER). *J. Am. Chem. Soc.* **2015**, *137*, 13031−13040.
(44) Tan, X.; Shen, J.; Semagina, N.; Secanell, M. Decoupling Structure-Sensitive Deactivation Mechanisms of Ir/IrOx Electrocatalysts toward Oxygen Evolution Reaction. *J. Catal.* **2019**, *371*, 57−70.
(45) Jung, S.; Mccrory, C. C. L.; Ferrer, I. M.; Peters, J. C.; Jaramillo, T. F. Benchmarking Nanoparticulate Metal Oxide Electrocatalysts for the Alkaline Water Oxidation Reaction. *J. Mater. Chem. A* **2016**, *4*, 3068−3076.

https://doi.org/10.1021/acsanm.2c00031
ACS Appl. Nano Mater. 2022, 5, 4062−4071

(46) Ren, H.; Pan, Y.; Sorrell, C. C.; Du, H. Assessment of Electrocatalytic Activity through the Lens of Three Surface Area Normalization Techniques. *J. Mater. Chem. A* **2020**, *8*, 3154−3159.
(47) Stevens, D. A.; Dahn, J. R. Electrochemical Characterization of the Active Surface in Carbon-Supported Platinum Electrocatalysts for PEM Fuel Cells. *J. Electrochem. Soc.* **2003**, *150*, A770−A775.
(48) Karimi, F.; Bazylak, A.; Peppley, B. A. Effect of Calcination Temperature on the Morphological and Electrochemical Characteristics of Supported Iridium Hydroxyoxide Electrocatalysts for the PEM Electrolyzer Anode. *J. Electrochem. Soc.* **2017**, *164*, F464−F474.
(49) Ooka, H.; Yamaguchi, A.; Takashima, T.; Hashimoto, K.; Nakamura, R. Efficiency of Oxygen Evolution on Iridium Oxide Determined from the PH Dependence of Charge Accumulation. *J. Phys. Chem. C* **2017**, *121*, 17873−17881.
(50) Liu, Y.; Zhang, L.; Willis, B. G.; Mustain, W. E. Importance of Particle Size and Distribution in Achieving High-Activity, High-Stability Oxygen Reduction Catalysts. *ACS Catal.* **2015**, *5*, 1560−1567.
(51) Wu, S.; Yu, B.; Wu, Z.; Fang, S.; Shi, B.; Yang, J. Effect of Particle Size Distribution on the Electrochemical Performance of Micro-Sized Silicon-Based Negative Materials. *RSC Adv.* **2018**, *8*, 8544−8551.
(52) Yano, H.; Watanabe, M.; Iiyama, A.; Uchida, H. Particle-Size Effect of Pt Cathode Catalysts on Durability in Fuel Cells. *Nano Energy* **2016**, *29*, 323−333.
(53) García, J. R.; Bidabehere, C. M.; Sedran, U. Non-Uniform Size of Catalyst Particles. Impact on the Effectiveness Factor and the Determination of Kinetic Parameters. *Chem. Eng. J.* **2020**, *396*, No. 124994.
(54) Trogadas, P.; Fuller, T. F. The Effect of Uniform Particle Size Distribution on Pt Stability. *ECS Trans.* **2011**, *41*, 761−773.
(55) Nong, H. N.; Gan, L.; Willinger, E.; Teschner, D.; Strasser, P. IrOx Core-Shell Nanocatalysts for Cost- and Energy-Efficient Electrochemical Water Splitting. *Chem. Sci.* **2014**, *5*, 2955−2963.
(56) Godínez-Salomón, F.; Albiter, L.; Alia, S. M.; Pivovar, B. S.; Camacho-Forero, L. E.; Balbuena, P. B.; Mendoza-Cruz, R.; Arellano-Jimenez, M. J.; Rhodes, C. P. Self-Supported Hydrous Iridium−Nickel Oxide Two-Dimensional Nanoframes for High Activity Oxygen Evolution Electrocatalysts. *ACS Catal.* **2018**, *8*, 10498−10520.
(57) Nong, H. N.; Reier, T.; Oh, H.-S.; Gliech, M.; Paciok, P.; Ha, T.; Vu, T.; Teschner, D.; Heggen, M.; Petkov, V.; Schlögl, R.; Jones, T.; Strasser, P. A Unique Oxygen Ligand Environment Facilitates Water Oxidation in Hole-Doped IrNiOx Core−Shell Electrocatalysts. *Nat. Catal.* **2018**, *1*, 841−851.
(58) Casalongue, H. G. S.; Ng, M. L.; Kaya, S.; Friebel, D.; Ogasawara, H.; Nilsson, A. InSitu Observation of Surface Species on Iridium Oxide Nanoparticles during the Oxygen Evolution Reaction. *Angew. Chem., Int. Ed.* **2014**, *53*, 7169−7172.
(59) Li, G.; Li, S.; Ge, J.; Liu, C.; Xing, W. Discontinuously Covered IrO2-RuO2@Ru Electrocatalysts for the Oxygen Evolution Reaction: How High Activity and Long-Term Durability Can Be Simultaneously Realized in the Synergistic and Hybrid Nano-Structure. *J. Mater. Chem. A* **2017**, *5*, 17221−17229.
(60) Nong, H. N.; Tran, H. P.; Spöri, C.; Klingenhof, M.; Frevel, L.; Jones, T. E.; Cottre, T.; Kaiser, B.; Jaegermann, W.; Schlögl, R.; Teschner, D.; Strasser, P. The Role of Surface Hydroxylation, Lattice Vacancies and Bond Covalency in the Electrochemical Oxidation of Water (OER) on Ni-Depleted Iridium Oxide Catalysts. *Z. Phys. Chem.* **2020**, *234*, 787−812.
(61) Antolini, E. Iridium As Catalyst and Cocatalyst for Oxygen Evolution/Reduction in Acidic Polymer Electrolyte Membrane Electrolyzers and Fuel Cells. *ACS Catal.* **2014**, *4*, 1426−1440.
(62) Li, G.; Li, S.; Xiao, M.; Ge, J.; Liu, C.; Xing, W. Nanoporous IrO 2 Catalyst with Enhanced Activity and Durability for Water Oxidation Owing to Its Micro/Mesoporous Structure. *Nanoscale* **2017**, *9*, 9291−9298.
(63) Park, J.; Sa, Y. J.; Baik, H.; Kwon, T.; Joo, S. H.; Lee, K. Iridium-Based Multimetallic Nanoframe@Nanoframe Structure: An Efficient and Robust Electrocatalyst toward Oxygen Evolution Reaction. *ACS Nano* **2017**, *11*, 5500−5509.
(64) Alia, S. M.; Rasimick, B.; Ngo, C.; Neyerlin, K. C.; Kocha, S. S.; Pylypenko, S.; Xu, H.; Pivovar, B. S. Activity and Durability of Iridium Nanoparticles in the Oxygen Evolution Reaction. *J. Electrochem. Soc.* **2016**, *163*, F3105−F3112.
(65) Oh, H. S.; Nong, H. N.; Reier, T.; Bergmann, A.; Gliech, M.; Ferreira De Araújo, J.; Willinger, E.; Schlögl, R.; Teschner, D.; Strasser, P. Electrochemical Catalyst-Support Effects and Their Stabilizing Role for IrOx Nanoparticle Catalysts during the Oxygen Evolution Reaction. *J. Am. Chem. Soc.* **2016**, *138*, 12552−12563.
(66) Huang, J.; Hörmann, N.; Oveisi, E.; Loiudice, A.; De Gregorio, G. L.; Andreussi, O.; Marzari, N.; Buonsanti, R. Potential-Induced Nanoclustering of Metallic Catalysts during Electrochemical CO2 Reduction. *Nat. Commun.* **2018**, *9*, No. 3117.
(67) Beermann, V.; Holtz, M. E.; Padgett, E.; De Araujo, J. F.; Muller, D. A.; Strasser, P. Real-Time Imaging of Activation and Degradation of Carbon Supported Octahedral Pt-Ni Alloy Fuel Cell Catalysts at the Nanoscale Using: In Situ Electrochemical Liquid Cell STEM. *Energy Environ. Sci.* **2019**, *12*, 2476−2485.
(68) Li, G.; Yu, H.; Wang, X.; Sun, S.; Li, Y.; Shao, Z.; Yi, B. Highly Effective IrxSn1-XO2 Electrocatalysts for Oxygen Evolution Reaction in the Solid Polymer Electrolyte Water Electrolyser. *Phys. Chem. Chem. Phys.* **2013**, *15*, 2858−2866.
(69) Urchaga, P.; Kadyk, T.; Rinaldo, S. G.; Pistono, A. O.; Hu, J.; Lee, W.; Richards, C.; Eikerling, M. H.; Rice, C. A. Catalyst Degradation in Fuel Cell Electrodes: Accelerated Stress Tests and Model-Based Analysis. *Electrochim. Acta* **2015**, *176*, 1500−1510.
(70) Kovács, A.; Schierholz, R.; Tillmann, K. FEI Titan G2 80-200 CREWLEY. *J. Large-Scale Res. Facil.* **2016**, *2*, A43.

https://doi.org/10.1021/acsanm.2c00031
ACS Appl. Nano Mater. 2022, 5, 4062−4071